A 10 MHz DC/DC Converter With Zero-Phase Difference Synchronous Driving Signal

Yueshi Guan, *Member, IEEE*, Zhenyu Shi, *Student Member, IEEE*, Chang Liu, *Student Member, IEEE*,
Yijie Wang, *Senior Member, IEEE*, and Dianguo Xu, *Fellow, IEEE*

***Abstract*—In this article, a 10 MHz dc/dc converter based on three-dimensional air core transformer with zero-phase difference synchronous driving signals is designed. By using the characteristics of no leakage inductance in the inner winding of the nested toroidal air core transformer, the phase difference between the output voltage of the inverter and the input voltage of the rectifier can be regarded as zero, so that the rectifier and the inverter can use the same driving signal, which simplifies the control of the synchronous rectifier switches, and realizes the reliable and efficient synchronous rectification control at 10 MHz. The prototypes with primary and secondary compensation are proposed and the experimental results verify the feasibility of the proposed control method and numerical design method.**

***Index Terms*—DC/DC, high frequency, nested toroidal air core transformer, synchronous rectification.**

I. INTRODUCTION

WITH THE continuous development of power electronic technology, the efficiency and volume of switching power electronic systems are significantly expected to be improved [1]–[8]. High operating frequency can reduce the necessary stored energy of passive components within every period, leading to small value and volume of transformer, inductor, and electrolytic capacitor. Thus, increasing operating frequency is the most effective way to reduce power converter volume. In addition, with the value reduction of passive components, the parasitic components are in the similar value of required resonant components. Therefore, increasing the operating frequency of the system cannot only reduce the volume of the system, but also use the parasitic components to absorb the resonant elements and reduce the number of components [9]–[13]. For example, when the frequency is raised to several and tens of MHz, the resonant inductor will be in the similar level of the leakage inductance of various air core transformers, so that the leakage inductance of various air core transformers can be further used as resonant elements to reduce the number of devices.

In high-frequency dc/dc converters, Schottky diodes are used in the rectifier stage normally because of the high switching speed characteristics. However, the forward voltage drop is still high. In order to improve the efficiency of high-frequency dc/dc converter, synchronous rectification technology has been more and more applied to switching power supply in recent years [14]–[17]. Due to MOSFET has a very low ON-resistance, the conduction loss can be reduced by turning on MOSFET within the ON time of Schottky diode [18], [19]. But one of the difficulties of synchronous rectification is to control the phase of the switch driving signal in the rectifier, especially under tens of MHz operating frequency conditions. Due to the existence of passive components, parasitic inductance and leakage inductance of transformer in resonant circuit, the phase difference between the input voltage of rectifier and the output voltage of inverter cannot be ignored. There are several challenges for synchronous driving under tens of MHz conditions. One challenge is that the phase difference cannot be calculated or measured accurately, the phase errors of driving signal will lead to the wrong action of synchronous rectifier switches, and the body diode may conduct and increase the reverse conduction loss in high-frequency applications [20]. Another challenge is that there is no available analog controller for synchronous rectification that can operate at such high frequency. Also, for digital driving, the accuracy of FPGA is not enough. In the case of low-power and low-voltage HF/VHF dc/dc power converters, [21] and [22] have demonstrated a self-driven gating method for synchronous rectifiers. However, these methods require additional resonant circuits, which make it difficult to drive synchronous rectifier switches accurately, especially around tens of MHz. So how to make synchronous rectification more accurate and efficient above tens of MHz is of great significance.

In order to solve this problem, the zero-phase difference characteristic is expected between primary side driving signal and secondary side synchronous driving signal. To achieve this performance, the nested toroidal air core transformer is adopted in this article [23], [24]. Based on the leakage free characteristics of the air core transformer, the phase difference between the input voltage of rectifier and the output voltage of inverter can be eliminated. Therefore, the rectifier and inverter can use the same driving signal without phase difference, which solves the challenges of synchronous rectification under tens of MHz.

Manuscript received December 21, 2020; revised March 14, 2021 and May 7, 2021; accepted May 25, 2021. Date of publication June 1, 2021; date of current version August 16, 2021. This work was supported in part by the National Natural Science Foundation of China under Grant 52007041, in part by the Power Electronics Science and Education Development Program of Delta Group under Grant DREG2020008, in part by the Natural Science Foundation of Heilongjiang Province under Grant LH2020E050, and in part by the Youth Talent Project of HIT. Recommended for publication by Associate Editor F. Costa. *(Corresponding author: Yueshi Guan.)*

The authors are with the School of Electrical Engineering and Automation, Harbin Institute of Technology, Harbin 150001, China (e-mail: hitguanyueshi @163.com; 649447536@qq.com; 18800428682@163.com; wangyijie@hit.edu.cn; xudiang@hit. edu.cn).

Color versions of one or more figures in this article are available at https://doi.org/10.1109/TPEL.2021.3084975.

Digital Object Identifier 10.1109/TPEL.2021.3084975

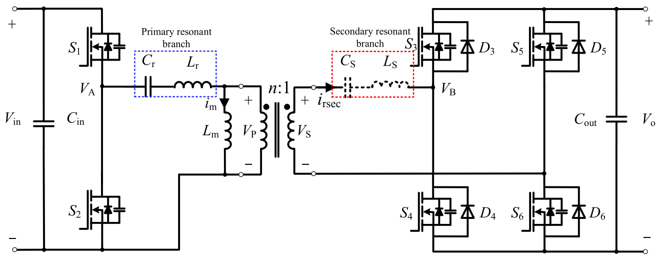

Fig. 1. Diagram of high-frequency converter based on Class DE inverter, transformer, resonant branch, and full-bridge synchronous rectifier.

In this article, a 50 V input, 12 V/28 W output prototype is proposed, which is an initial attempt for an intermediate bus converter for satellite power conversion system. Meanwhile, for other DCX applications, the proposed topology can also be applied and step-down ratio can be improved.

The rest of this article is organized as follows. Section II analyzes the proposed topology and analyzes the relationship between the resonant elements and the phase difference of rectifier and inverter, the parameter design method of topology is also introduced in Section II. In section III, the nested toroidal air core transformer is analyzed and designed. Furthermore, the transformer is simulated by MAXWELL and manufactured by three-dimensional (3-D) copper casting. In Section IV, the experimental results of nested toroidal air core transformer and planar air core PCB transformer with and without synchronous rectification are compared. Finally, Section V concludes this article.

II. ANALYSIS OF PROPOSED CONVERTER AND THE INFLUENCE OF RESONANT ELEMENT ON DRIVING SIGNAL CONTROL

The circuit diagram of high-frequency converter is shown in Fig. 1. It consists of a Class DE inverter, an LC series resonant branch (either in the primary side or secondary side), a transformer, and a full-bridge synchronous rectifier. The Class DE inverter converts the dc component to ac component. The LC series branch and transformer form a matching network. The synchronous rectifier converts the ac component to dc component. The main input power stage consists of S_1 and S_2. A transformer is used to absorb resonant inductors, providing electrical isolation as well as stepping down the input voltage. Here, take the resonant branch in the primary side as an example. The power is transmitted from the input side to the output side through the resonance of L_r and C_r. Hence, the current flowing through the resonant tank can be approximately regarded as a sinusoidal shape. Based on the fundamental harmonic approximation, the ac equivalent circuit of the Class DE converter is shown in Fig. 2.

R_{ac} is the equivalent resistance of rectifier and transformer, which can be calculated by the following equation [25]:

$$R_{\mathrm{ac}} = n^2 r_{\mathrm{ac}} = n^2 \frac{8R_L}{\pi^2} \tag{1}$$

where r_{ac} is the equivalent resistance of rectifier, R_{L} is the load resistance, and n is the transformer ratio.

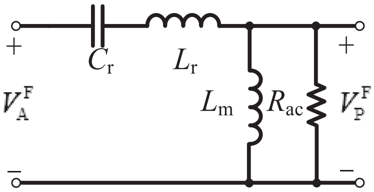

Fig. 2. AC equivalent circuit of the resonant tank based on FHA.

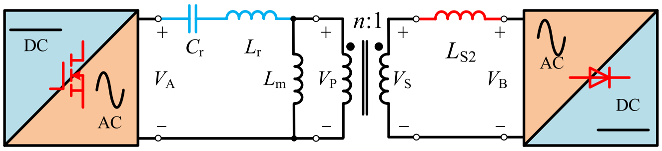

Fig. 3. Simplified equivalent circuit diagram of the proposed topology after the transformer is equivalent.

The gain M of the circuit can be calculated as follows [26]:

$$M = \frac{K}{\sqrt{\left(1 + K - \frac{1}{f_n^2}\right)^2 + Q^2K^2\left(f_{\mathrm{n}} - \frac{1}{f_n}\right)^2}} \tag{2}$$

where K is the inductance factor, f_r is the resonant frequency of L_r and C_r, f_n is the normalized frequency, Q is the quality factor, $K = L_m/L_r$, $f_r = 1/2\pi\sqrt{L_r C_r}$, $f_n = f_s/f_r$. f_s is the switching frequency, and $Q = 2\pi f_r L_r / R_{\mathrm{ac}}$.

Large magnetizing inductance (L_m) limits the charging and discharging speed of the output capacitor of the switch, thus affecting the soft switching. So in order to ensure ZVS, the magnetizing inductance L_m needs to satisfy the following inequality [27]:

$$L_m \le \frac{T_d}{8 f_s C_{\mathrm{oss}}} \tag{3}$$

where T_d and C_{oss} are the dead time and the output capacitance of switch, respectively.

For the conventional air core transformer, due to its low coupling coefficient, large leakage inductance will be introduced into the primary and secondary sides. In high-frequency case, the leakage inductance value is close to the resonant element in the circuit, so it can be used as the resonant element to participate in resonance. In the above resonant tank, the primary side leakage inductance L_{S1} can be used as the resonant inductor L_r to resonate with the resonant capacitor C_r at the frequency f_r. The secondary leakage inductance L_{S2} is connected in series between the output of transformer and the full-bridge rectifier, as shown in Fig. 3.

Usually when design resonant tank, the resonant frequency f_r of L_r and C_r can be designed to be the same as the switching frequency f_S. At this time, for the fundamental wave, the phase difference of V_A, V_P, and V_S can be regarded as zero because L_r and C_r are in series resonance. However, due to the existence of secondary leakage inductance L_{S2}, the phase difference between

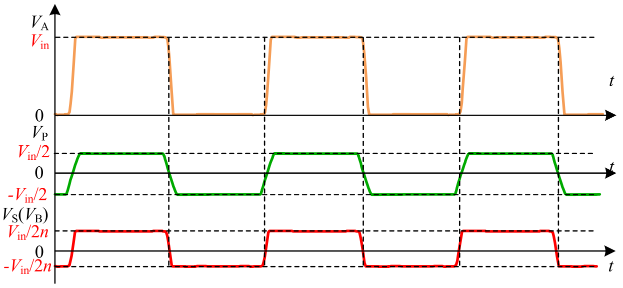

Fig. 4. Waveform diagram of V_A, V_P, V_S, and V_B when there is no leakage inductance on the secondary side of transformer.

V_A and V_B can be calculated as follows:

$$\Delta\theta = \theta_{V_A} - \theta_{V_B} = \arctan\left(\frac{2\pi f_S L_{S2}}{r_{\mathrm{ac}}}\right). \tag{4}$$

Therefore, for synchronous rectification of the rectifier bridge, it is necessary to accurately control the phase difference between the inverter and rectifier drive signals, but with the increment of the working frequency of the system, the time of each cycle becomes shorter and shorter, which makes the control of driving signal more and more difficult. In theory, the phase difference can be compensated by making C_r not resonate with L_r at the switching frequency. However, under this design condition, many parameters affect the value of C_r, such as L_m, n, L_{S2}, and L_r. These parameters need to be very accurate and small deviations cause large error, leading to large phase difference between the primary side and secondary side. Therefore, the existence of leakage makes the control of driving signal more stringent, especially in the case of tens of MHz.

As a result, if the leakage inductance of one side can be eliminated, the phase difference between V_A and V_B can be regarded as zero. When the load changes, the phase difference will be kept at zero, so it is not necessary to adjust. The rectifier and inverter can use the same driving signal, which simplifies the control of synchronous rectifier driving signal and improves the controllability and efficiency of synchronous rectification.

In this case, for the selected input voltage V_{in}, the waveforms of V_A, V_P, V_S, and V_{B} are shown in Fig. 4. The input voltage of rectifier V_B can be regarded as a square wave voltage with duty cycle of 0.5 and amplitude of $\pm V_{\mathrm{in}}/2n$, resulting in the output voltage after rectification is almost $V_{\mathrm{in}}/2n$. The transformer ratio is

$$n = V_{\mathrm{in}}/2V_{\mathrm{o}}. \tag{5}$$

The coupling coefficient of various air core transformers is generally low; therefore, when the inductance coefficient K is about 0.7, it is easier to design the following air core transformer. After the transformer designed, the value of resonance capacitance C_r can be determined by the following equation, according to the designed primary side leakage inductance L_r of the transformer:

$$C_r = \frac{1}{(2\pi f_S)^2 L_r}. \tag{6}$$

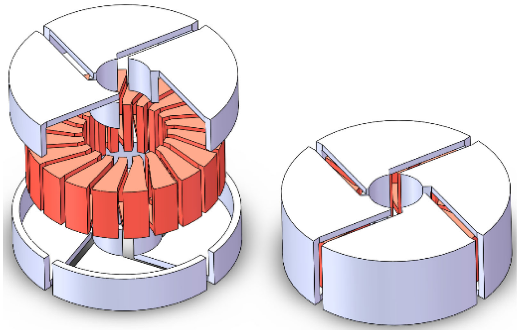
(a) (b)

Fig. 5. Schematic diagram of nested toroidal air core transformer. (a) Structural division diagram. (b) Overall structure diagram.

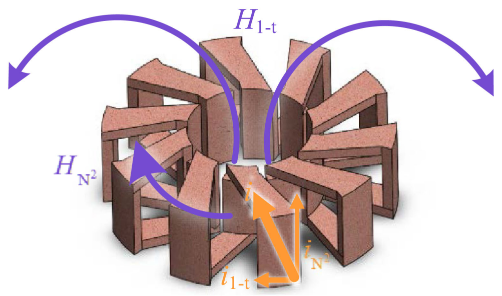

Fig. 6. Total current can be divided into the radial current i_{N2} and the circumferential current i_{1-t}. They contribute to the enclosed field H_{N2} and H_{1-t}, respectively.

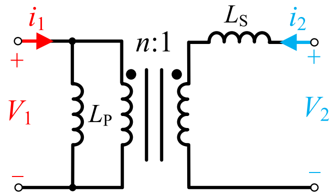

Fig. 7. Equivalent schematic of nested toroidal air core transformer.

III. ANALYSIS, DESIGN, AND MANUFACTURE OF NESTED TOROIDAL AIR CORE TRANSFORMER

The schematic diagram of nested toroidal air core transformer is shown in Fig. 5. Fig. 5(a) shows its structural subdivision and Fig. 5(b) shows the overall structure. The nested toroidal air core transformer has two windings with one surrounding the other. In this case, both windings couple their N^2 magnetic fields shown in Fig. 6. Moreover, the magnetic flux leakage of the inner cross section is closed by the outer cross section, so the magnetic flux leakage of the inner winding can be regarded as zero, which is explained in following content, and the magnetic flux leakage of the outer winding can be controlled by adjusting the distance between the inner and outer windings. The transformer can be equivalent to the circuit diagram shown in Fig. 7 (the red internal winding is the input side) to eliminate leakage inductance.

In Fig. 7, L_S is the leakage inductance and L_P is the magnetic inductance of the proposed transformer (which is in the primary

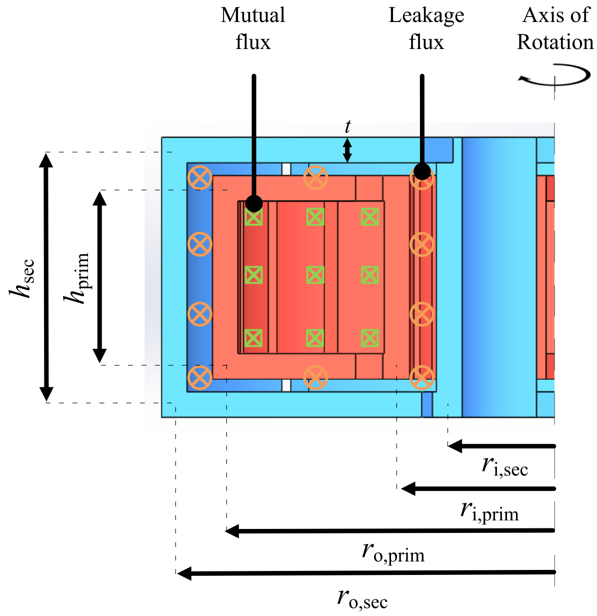

Fig. 8. Cross section diagram of the nested todoidal air core transformer shows the leakage flux in the yellow part and the mutual flux in the blue part. Red inner winding is the primary winding and the blue outer winding is the secondary winding.

side and can also be transferred to the secondary side). n is the transformer ratio. In order to calculate L_P, L_S, and n in the equivalent circuit, the mutual reluctance $\Re_m$ caused by the common flux path of the internal and external windings as well as the leakage reluctance $\Re_{l2}$ caused by the flux path inside the outer winding but outside the inner winding as shown in Fig. 8 should be calculated first.

Using Ampere' law in (7), the expression for the H-field inside the toroid ($H = Ni/2\pi r$) can be obtained, where N is the number of turns of the toroid and i is the current. Then, the surface integral of the H-field inside of the inner cross section and the area between the inner and outer cross section provides the mutual flux Φ_m and the leakage flux Φ_{l2} respectively. Then, $\Re_m$ and $\Re_{l2}$ can be calculated by (8) and (9)

$$\oint_{c} B \cdot dl = \mu_0 I_{\text{enc}} \tag{7}$$

$$\Re_m = \frac{Ni}{\Phi_m} = \frac{Ni}{\int \mu_0 H dS} = \frac{Ni}{\mu_0 \left(h_{\text{prim}} - t\right) \int_{r_{i,\text{prim}}+\frac{t}{2}}^{r_{o,\text{prim}}-\frac{t}{2}} \frac{Ni}{2\pi r} dr}$$
$$= \frac{2\pi}{\mu_0 \left(h_{\text{prim}} - t\right) \ln\left(\frac{r_{o,\text{prim}}-\frac{t}{2}}{r_{i,\text{prim}}+\frac{t}{2}}\right)} \tag{8}$$

$$\Re_{l2} = \frac{Ni}{\Phi_2 - \Phi_m} =$$
$$\frac{Ni}{\mu_0 \left(h_{\text{sec}} - t\right) \int_{r_{i,\text{sec}}+\frac{t}{2}}^{r_{o,\text{sec}}-\frac{t}{2}} \frac{Ni}{2\pi r} dr - \mu_0 \left(h_{\text{prim}} + t\right) \int_{r_{\text{i,prim}}-\frac{t}{2}}^{r_{\text{o,prim}}+\frac{t}{2}} \frac{Ni}{2\pi r} dr}$$
$$= \frac{2\pi}{\mu_0 \left[\left(h_{\text{sec}} - t\right) \ln\left(\frac{r_{o,\text{sec}}-\frac{t}{2}}{r_{i,\text{sec}}+\frac{t}{2}}\right) - \left(h_{\text{prim}} + t\right) \ln\left(\frac{r_{o,\text{prim}}+\frac{t}{2}}{r_{i,\text{prim}}-\frac{t}{2}}\right)\right]}. \tag{9}$$

The area of the inner coil flux is the same as that of the inner and outer coils, so it can be considered that the inner coil flux contributes to the common flux completely, and there is no magnetic leakage, so the leakage inductance of the inner winding is zero.

Once the reluctance values are known, the inductance matrix can be obtained as shown in the following:

$$\begin{bmatrix} \Psi_1 \\ \Psi_2 \end{bmatrix} = \begin{bmatrix} N_1 \Phi_1 \\ N_2 \Phi_2 \end{bmatrix} = \begin{bmatrix} L_{11} & L_{\bar{M}} \\ L_M & L_{22} \end{bmatrix} \begin{bmatrix} i_1 \\ i_2 \end{bmatrix}$$
$$= \begin{bmatrix} \frac{N_1^2}{\Re_m} & \frac{N_1 N_2}{\Re_m} \\ \frac{N_1 N_2}{\Re_m} & \frac{N_2^2}{\Re_m} + \frac{N_2^2}{\Re_{l2}} \end{bmatrix} \begin{bmatrix} i_1 \\ i_2 \end{bmatrix}$$
$$= \begin{bmatrix} L_P & \frac{L_P}{n} \\ \frac{L_P}{n} & \frac{L_P}{n^2} + L_S \end{bmatrix} \begin{bmatrix} i_1 \\ i_2 \end{bmatrix}. \tag{10}$$

The inductance matrix provides the transformation between various transformer models, and (10) expresses the matrix using parameters (L_P, L_S, and n).

But formula (10) neglects the inductance and coupling produced by one-turn magnetic fields of the toroids. Therefore, in order to further improve the accuracy of the inductance matrix, L_{11} and L_{22} should increase one-turn inductance of primary and secondary toroids caused by current $i_{1\&\text{minus};t}$ in Fig. 6, respectively. The formula (11) for calculating L_{1-t-1} and L_{1-t-2} is as follows [28]:

$$L_{1-t-x} = \frac{d_{o-x} + d_{i-x}}{4} \mu_0 \left[\ln\left(8 \frac{d_{o-x} + d_{i-x}}{d_{o-x} - d_{i-x}}\right) - 2\right]$$
$$x = 1, 2 \tag{11}$$

where d_{o-x} and d_{i-x} are the outer diameter and inner diameter of the coils, respectively.

As a result, the inductance matrix can be modified to

$$\begin{bmatrix} L_{11} & L_M \\ L_M & L_{22} \end{bmatrix} = \begin{bmatrix} \frac{N_1^2}{\Re_m} + L_{1-t-1} & \frac{N_1 N_2}{\Re_m} \\ \frac{N_1 N_2}{\Re_m} & \frac{N_1^2}{\Re_m} + \frac{N_2^2}{\Re_{l2}} + L_{1-t-2} \end{bmatrix}$$
$$= \begin{bmatrix} L_P & \frac{L_P}{n} \\ \frac{L_P}{n} & \frac{L_P}{n^2} + L_S \end{bmatrix}. \tag{12}$$

The expression of the parameters (L_P, L_S, and n) in Fig. 7 can be deduced from (10) as follows:

$$\begin{cases} L_P = L_{11} \quad L_S = \left(1 - k^2\right) L_{22} \\ k = \frac{L_M}{\sqrt{L_{11} L_{22}}} \quad n = \frac{L_{11}}{L_M} = \frac{N_1}{N_2} \end{cases} \tag{13}$$

where k is the coupling coefficient of the proposed transformer.

From (12) and (13), it can be known that the transformer ratio can be changed by adjusting the number of primary and secondary side turns. The transformer can be used as a step-up transformer if the transformation ratio is less than one, and the transformer can be used as a step-down transformer if the transformation ratio is greater than one. It depends on the application fields.

In this article, a step-down converter is analyzed and a transformer prototype is built, the design parameters of the proposed

TABLE I
PARAMETERS OF TRANSFORMER INNER AND OUTER WINDING

Parameters	Primary winding (Inner winding)	Secondary winding (Outer winding)
Outer diameter[mm]	52	60
Inner diameter[mm]	25	17
Height[mm]	14	20
Thickness[mm]	2	2
Separation distance[mm]	2	2
Number of turns	20	4

TABLE II
COMPARISON OF INDUCTANCE MATRIX VALUES AND PARAMETERS (L_P, L_S, AND N) BETWEEN CALCULATION, MAXWELL SIMULATION, AND EXPERIMENT

Variable	Calculation	Simulation	Experiment
L_{11}[nH]	618.8	663.0	664.5
L_M[nH]	118.3	139.3	140.5
L_{22}[nH]	60.3	75.6	73.5
L_P[nH]	618.8	663.0	664.5
L_S [nH]	37.7	46.3	43.8
n	5.23	4.76	4.73
k	0.613	0.622	0.636

transformer are shown in Table I. Taking the transformer for example, the corresponding parameters can be calculated as follows.

From (8) and (9), $\Re_m$ and $\Re_{12}$ can be calculated as follows:

$$\begin{cases} \Re_m = 6.76 \times 10^8 \mathrm{H}^{-1} \\ \Re_{12} = 7.77 \times 10^8 \mathrm{H}^{-1}. \end{cases} \tag{14}$$

Next, the parameters in Table I are brought into formula (11) to calculate the one-turn inductance of primary and secondary toroids, respectively. The calculation results are as follows:

$$\begin{cases} L_{1-t-1} = 27.3\,\mathrm{nH} \\ L_{1-t-2} = 16.0\,\mathrm{nH}. \end{cases} \tag{15}$$

Last, using these reluctance values, N_1, N_2, L_{1-t-1}, and L_{1-t-2}, the inductance matrix can be obtained through (12)

$$\begin{bmatrix} L_{11} & L_M \\ L_M & L_{22} \end{bmatrix} = \begin{bmatrix} 618.8\,\mathrm{nH} & 118.3\,\mathrm{nH} \\ 118.3\,\mathrm{nH} & 60.3\,\mathrm{nH} \end{bmatrix}. \tag{16}$$

For the inductance generated by i_{1-t}, on the one hand, the calculated additional inductance L_{1-t-1} is 27.3 nH, while L_{11} is 618.8 nH, and the difference between them is 20 or 30 times. Also, the primary and secondary windings have both current and magnetic field in this direction, and there is coupling between them. Therefore, there must be some mutual inductance in L_{1-t-1} and L_{1-t-2}, which makes the leakage inductance far different from L_{11}. So the leakage inductance caused by L_{1-t-1} can be ignored, which is far less than self-inductance (more than 20 times).

According to the design parameters in Table I, the model is established and simulated in Maxwell. The transformer parameters obtained by simulation are shown in Table II. The distribution diagrams of magnetic field intensity obtained by simulation are shown in Fig. 9.

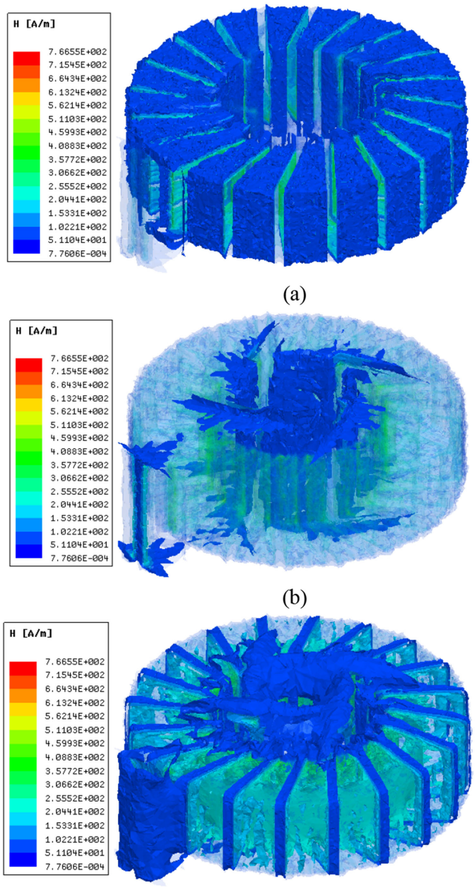

(a)

(b)

(c)

Fig. 9. Magnetic field distribution diagrams of transformer obtained by MAXWELL simulation. (a), (b), and (c) show the magnetic fields of the inner winding, outer winding, and air, respectively. (a) Distribution diagram of magnetic field intensity in inner winding. (b) Distribution diagram of magnetic field intensity in outer winding. (c) Distribution diagram of magnetic field intensity in the air.

It can be seen that almost all the magnetic flux is confined in the outer winding, and there is almost no magnetic leakage outside the outer winging. This proves that the magnetic flux leakage of the inner cross section is closed by the outer cross section, so the magnetic flux leakage of the inner winding can be regarded as zero.

In addition, since the outer winding completely covers the inner winding, in order to facilitate the manufacture and installation of the transformer, we can adopt the two manufacturing methods shown in Fig. 10. Both of them can be fabricated by 3-D copper printing or copper casting combined with PCB.

Because of the large number of turns in inner winding, when the first method is adopted, there are many welding pads in the narrow space inside. At the same time, some errors are easy to appear in the welding position. The number of turns in the inner winding is more, and the error will have a certain influence on the characteristics. Although the second method is expensive to manufacture inner winding, it is better to adopt the second method.

Compared with the manufacturing method of 3-D printing and electroplating fabrication methodology, using 3-D copper

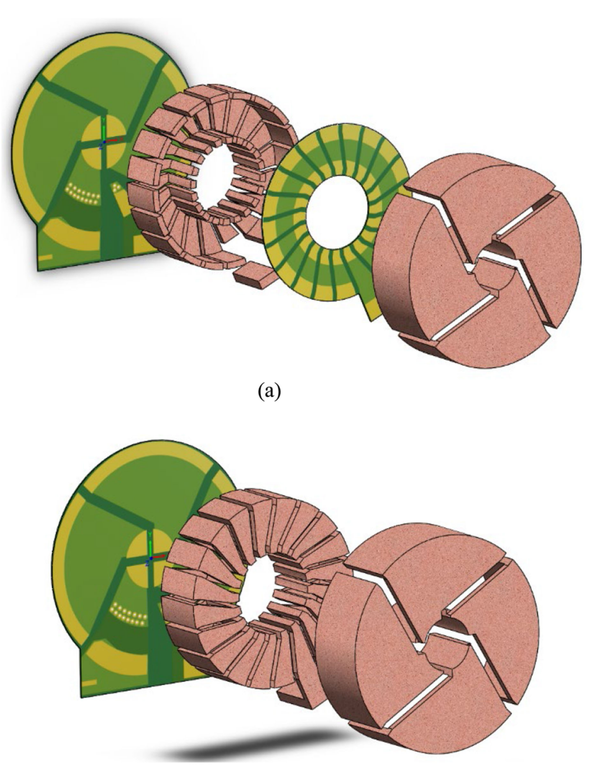

(a)

(b)

Fig. 10. Two manufacturing methods of nested toroidal air core transformer. (a) One side of the inner winding and outer winding is printed with PCB, and the remaining parts are printed with 3-D copper or copper casting. (b) One side of the outer winding is printed with PCB, and the remaining parts are printed with 3-D copper or copper casting.

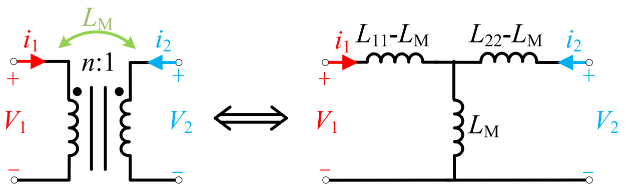

Fig. 11. Another equivalent circuit diagram of transformer.

printing or copper casting can improve the strength and thermal stability of the transformer, which can be used in harsh environment.

After the transformer is manufactured, in order to obtain the parameters (L_P, L_S, and n) of the transformer in Fig. 7 by test, $L_{1,\mathrm{open}}$, $L_{2,\mathrm{open}}$, and $L_{2,\mathrm{short}}$ should be measured separately, where $L_{1,\mathrm{open}}$ represents the inductance measured at the primary side when the secondary side is open, $L_{2,\mathrm{open}}$ represents the inductance measured at the secondary side when the primary side is open, and $L_{2,\mathrm{short}}$ represents the inductance measured at the secondary side when the primary side is short. In this article, we use an impedance analyzer named Keysight E4990A to mesure $L_{1,\mathrm{open}}$, $L_{2,\mathrm{open}}$, and $L_{2,\mathrm{short}}$ by frequency sweep.

For the equivalent circuit diagram of transformer shown in Figs. 7 and 11, $L_{1,\mathrm{open}}$, $L_{2,\mathrm{open}}$, and $L_{2,\mathrm{short}}$ can be calculated by (17) and (18), respectively, and (19) can be obtained by combining (17) and (18). Equation (19) gives the numerical relationship between measured values ($L_{1,\mathrm{open}}$, $L_{2,\mathrm{open}}$, and $L_{2,\mathrm{short}}$) and parameters(L_P, L_S, and n), (12) can also be derived from (19).

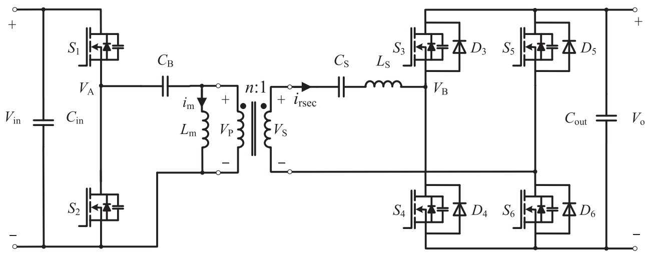

Fig. 12. High-frequency converter with secondary side compensation.

$$\begin{cases} L_{1,\mathrm{open}} = L_P \\ L_{2,\mathrm{open}} = L_S + \frac{L_P}{n^2} \\ L_{2,\mathrm{short}} = L_S \end{cases} \tag{17}$$

$$\begin{cases} L_{1,\mathrm{open}} = L_{11} \\ L_{2,\mathrm{open}} = L_{22} \\ L_{2,\mathrm{short}} = L_{22} - L_M + (L_{11} - L_M) \parallel L_M \end{cases} \tag{18}$$

$$\begin{cases} L_P = L_{11} \\ L_S = \left(1 - k^2\right) L_{22} \\ n = \frac{L_{11}}{L_M} \\ k = \frac{L_M}{\sqrt{L_{11} L_{22}}} \end{cases} \tag{19}$$

where k is the coupling coefficient.

Table II compares the inductance matrix values and parameters (L_P, L_S, and n) between calculation, MAXWELL simulation, and experiment. The results show that the theoretical calculation, simulation, and experimental results are in good agreement. Except that the calculated mutual inductance L_{12} and L_{21} is slightly lower than the simulated and experimental values because the coupling of the one-turn fields is ignored. The calculated self-inductance L_{11} and L_{22} is slightly lower than the simulated and experimental values which may be caused by the edge effects and other nonideal factors.

IV. EXPERIMENTAL RESULTS

A 10 MHz prototype with 24 V input voltage is built based on the proposed topology and transformer as shown in Fig. 12. For half bridge structure, there is dc component in the resonant tank of the primary side, thus, a capacitor C_B for dc blocking is necessary. In order to ensure that the phase of inverter output voltage V_A and rectifier input voltage V_B is the same, a capacitor C_S which resonates with L_S at switching frequency is also needed. All experimental parameters of this prototype are listed in Table III.

Fig. 13 shows the waveform of inverter output voltage V_A and rectifier input voltage V_B. It can be seen that the phase difference between inverter output voltage and rectifier input voltage is approximately zero when L_S and C_S are in series resonance at switching frequency and nested toroidal air core transformer with almost no leakage inductance on the primary

TABLE III
EXPERIMENTAL PARAMETERS OF THE PROTOTYPE

Device label	Value	Type
C_B	1μF	C1812X105K251T 1K
C_S	5.6nF	CC1206JRNPO9BN562
L_S	43.8nH	Secondary leakage inductance
n	4.73	Transformer ratio
R_L	1Ω	IT8511A+
Gate Drive	LMG1210RVRT	TEXAS INSTRUMENTS
S_1,S_2	EPC2010C	EPC
S_3,S_4, S_5,S_6	EPC2001C	EPC
D_3, D_4, D_5, D_6	SVM1045V2	PANJIT

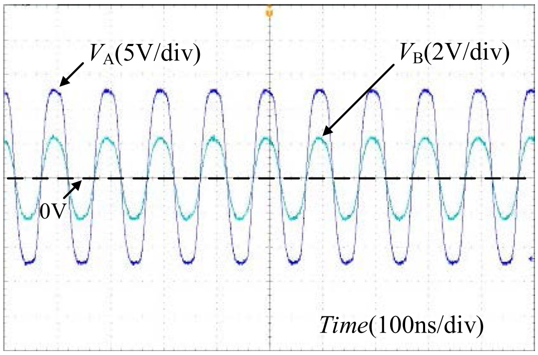

Fig. 13. Waveform of inverter output voltage V_A and rectifier input voltage V_B when the converter works under rated condition.

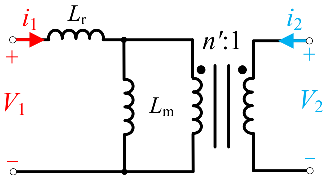

Fig. 14. Equivalent circuit diagram of transformer.

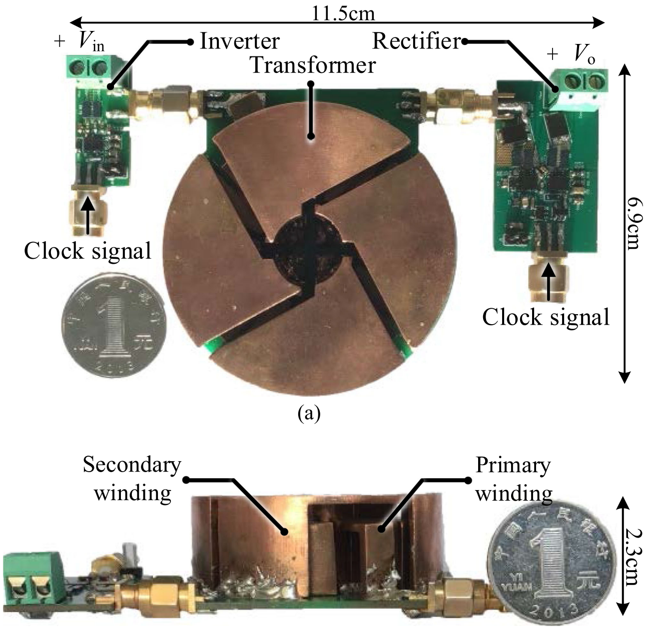

(a)

(b)

Fig. 15. Photographs of proposed converter. (a) Top view of the full system. (b) Side view of the full system.

side is used. Once the phase of V_A and V_B is the same, the same clock signal can be used to control the rectifier to realize synchronous rectification, which reduces the difficulty of high-frequency synchronous rectification.

When the secondary side with leakage inductance uses C_S to compensate L_S, it can make full use of the characteristic of no leakage inductance in the inner winding of nested toroidal transformer, but the primary side needs to add the capacitance C_B for dc blocking. A simplified circuit can be achieved by compensating on the primary side. Thus, a 10 MHz, 12 V/28 W with 50 V input voltage prototype is built based on the primary compensation and design method, which helps to verify the feasibility and correctness of the above design method.

To simplify the circuit, the LC series branch (L_r and C_r) is placed on the primary side as shown in Fig. 1. The model in Fig. 7 can be equivalent to the model in Fig. 14. The parameter conversion formula is shown as follows:

$$\begin{cases} L_r = \frac{n^2 L_S L_P}{n^2 L_S + L_P} \\ L_m = \frac{L_P^2}{n^2 L_S + L_P} \\ n' = \frac{n L_P}{n^2 L_S + L_P}. \end{cases} \tag{20}$$

The photograph of proposed converter is shown in Fig. 15. The transformer adopts the second manufacturing method shown in Fig. 10(b), that is, the inner winding is cast with copper as a whole, the bottom surface of the outer winding is made of PCB, and the rest is divided into four U-grooves and welded to the PCB.

In practice, the thickness of copper is expected to be far more than twice of the skin depth, which can greatly reduce the resistance. For the skin depth of copper at 10 MHz is tens of μm, as well as limit by the production process and also ensure the sturdiness of the structure, the copper thickness used in this article is initially determined as mm level. Also, the copper thickness has an impact on the parameters of the transformer. Thus, 2 mm copper thickness is selected by calculation which can achieve desired transformer parameters.

Furthermore, the photograph of the Class DE inverter circuit board with components labeled is shown in Fig. 16 and the photograph of the synchronous rectification circuit board with components labeled is shown in Fig. 17. The prototype occupies an area of 11.5×6.9 cm^2 and its vertical height is 2.3 cm. DPO4014B (Tektronix) is used as the oscilloscope in the experiment, the voltage probe is P6139A (Tektronix), the voltage source is DP832A (RIGOL).

Six driving signals of S_1, S_2 in inverter, S_3, S_4, S_5, and S_6 in rectifier should meet 1, 3, 6 in-phase and inverse with 2, 4, 5. Also, clock signal is expected to have extremely low

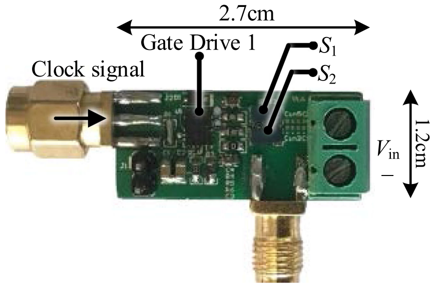

Fig. 16. Photograph of the Class DE inverter circuit board with components labeled.

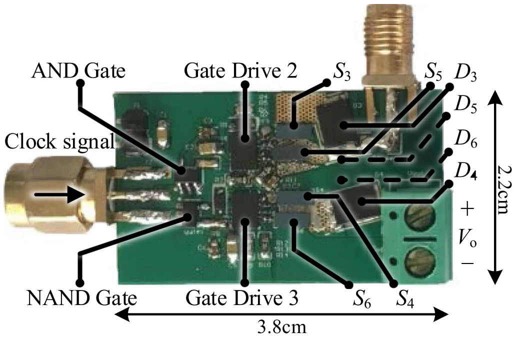

Fig. 17. Photograph of the synchronous rectification circuit board with components labeled.

TABLE IV
EXPERIMENTAL PARAMETERS OF THE PROTOTYPE

Device label	Value	Type
C_r	660pF	C1608C0G2E221JT000N*3
L_r	396nH	Primary leakage inductance
n'	1.91	Transformer ratio
R_L	5Ω	IT8511A+
Gate Drive	LMG1210RVRT	TEXAS INSTRUMENTS
S_1,S_2	EPC2010C	EPC
S_3,S_4, S_5,S_6	EPC2001C	EPC
D_3, D_4, D_5, D_6	SVM1045V2	PANJIT

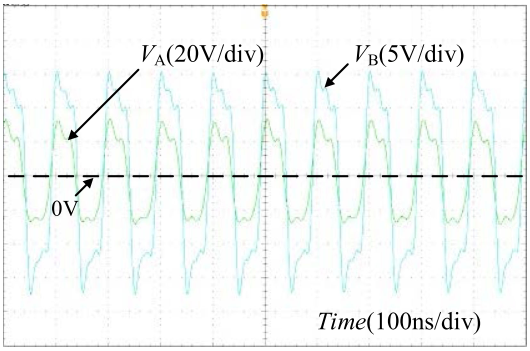

Fig. 18. Waveform of inverter output voltage V_A and rectifier input voltage V_B when the converter works under rated condition.

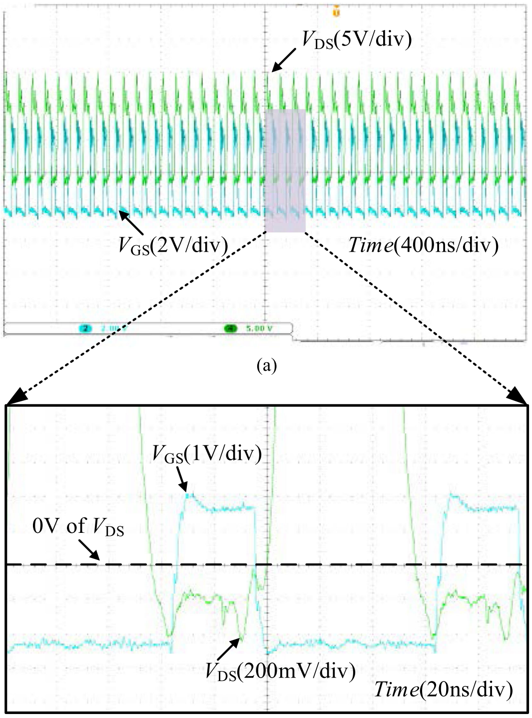

(a)

(b)

Fig. 19. Voltage waveform and driving signal waveform of the switch and its parallel Schottky diode.

delay after passing through the drive circuit, thus, three drive chips LMG1210RVRT, one extremely low delay AND gate NV7SZ08M5X, and one extremely low delay NAND gate NC7S00M5X are used. All experimental parameters of this prototype are listed in Table IV.

The waveforms of the prototype under rated working condition ($V_{\text{in}} = 50$ V, $V_{\text{out}} = 12$ V, $R_L = 5\ \Omega$) are shown in Figs. 18 and 19. Fig. 18 shows the waveform of inverter output voltage V_A and rectifier input voltage V_B when the converter works under rated condition. It can be seen that the phase difference between inverter output voltage and rectifier input voltage is approximately zero when L_r and C_r are in series resonance at switching frequency and nested toroidal air core transformer with almost no leakage inductance on the secondary side is used. Fig. 18 shows the voltage waveform and driving signal waveform of the switch and its parallel Schottky diode in this case. In order to better observe the effect of synchronous rectification, Fig. 19(a) is zoomed to obtain Fig. 19(b).

It can be clearly seen from Fig. 19(b) that with the zero-phase difference driving signal, the switch can be turned ON when the current flowing from source to drain, so that the forward voltage drop compared with Schottky diode is significantly reduced, which proves the feasibility of the proposed method.

Fig. 20 shows a planar air core PCB transformer with a similar magnetic inductance as the proposed transformer but there is certain leakage inductance on the secondary side. The primary and secondary side coils of the transformer are made of two PCBs. The primary side adopts four layer board with four turns of coils and the secondary side adopts two layer board with two turns of coils. The shape of six turns of coils is the same, the

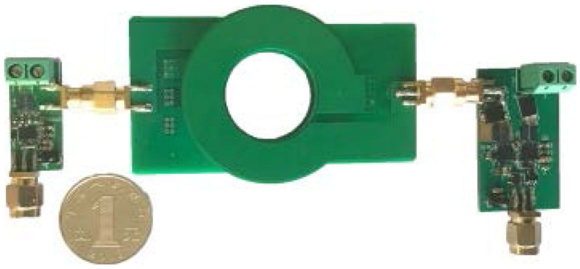

Fig. 20. Prototype with a planar air core PCB transformer.

TABLE V
PARAMETERS OF PLANAR AIR CORE TRANSFORMER

Parameter	Value
L_r	336.4nH
L_m	298.6nH
L_{S2}	87.9nH

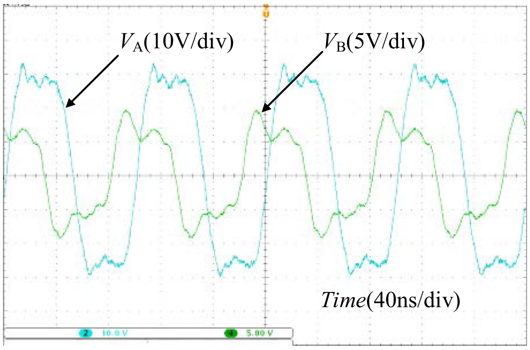

Fig. 21. Inverter output voltage and rectifier input voltage of the prototype with a planar air core PCB transformer.

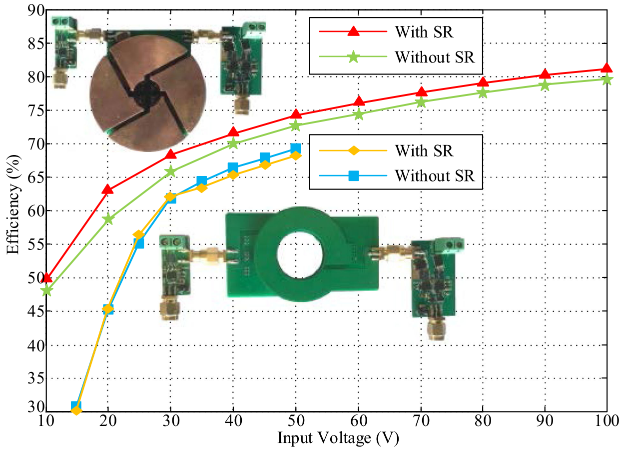

Fig. 22. Efficiency curve of the proposed topology using nested todoidal air core transformer and planar air core transformer measured by with and without synchronous rectification under different input voltage and power situations.

coil width is 10 mm and the thickness is 2 oz. At this time, the transformer transformation ratio is about 2. The parameters are shown in Table V.

Because of the leakage inductance of the secondary side, the output voltage will decrease and the phase difference between the output voltage of the inverter and the input voltage of the rectifier can be obtained as follows:

$$\Delta\theta = \arctan\left(\frac{2\pi \times 10 \times 10^6 \times 87.9 \times 10^{-9}}{8 \times 5/\pi^2}\right) = 54^\circ. \quad (21)$$

Fig. 21 shows the waveform of inverter output voltage and rectifier input voltage. It can be seen that the phase difference is about 60° due to the existence of L_{S2}. Two channels of 10 MHz signals with 60° phase difference are generated by FPGA to drive the inverter and rectifier switch, respectively.

Fig. 22 shows the efficiency curves of the proposed topology using nested toroidal air core transformer and planar air core PCB transformer measured by with and without synchronous rectification under different input voltage and power situations.

For the topology using nested toroidal air core transformer, with the rated input voltage of 50 V, the system output voltage is 11.75 V, the output power is 28.8 W, and the system efficiency is 74.5%. The efficiency of the prototype increases by 1.5% with synchronous rectification. It can be seen from Fig. 22 that when the input voltage continues to increase, the efficiency is still improved. When the input voltage is 100 V, the output power is up to 115 W and the efficiency is 81.1%. However, due to the large magnetic inductance of the designed transformer, the charging and discharging speed of the switch output capacitor is limited, which hinders the realization of the ZVS and limits the further improvement of the efficiency. In the future, the nested toroidal air core transformer with smaller magnetic inductance can be used for further improvement. Meanwhile, the proposed converter is designed as DCX with constant voltage conversion ratio. Thus, there is no close-loop control for the output voltage. In the future, the duty cycle and frequency can be adjusted to achieve close-loop control.

For the topology using planar air core PCB transformer, it can be seen from Fig. 22 that the efficiency with synchronous rectification is not obviously improved compared with diode rectification method, and even lower under high input voltage situations. It means that it is quite difficult to generate accurate synchronous driving signal at such high operating frequency. When the primary and secondary sides have large phase difference, the method of directly setting the phase difference leads to inaccurate switch action and decrease the system efficiency.

For the proposed topology, the converter power loss can be mainly divided into the inverter loss P_{inv}, the rectifier loss P_{rec}, the transformer loss P_{tra}, and the drive loss P_{dri}. The inverter loss mainly consists of conduction loss and switching loss.

The conduction loss of the switch can be obtained by [29]

$$P_{\text{cond}} = I_s^2 R_{\text{DSon}} \quad (22)$$

where R_{DSON} is the ON-state resistance of the switch. I_s is the current rms value flowing through the switch.

The switching loss can be calculated by the following [30]:

$$P_{\text{sw}} = (V_{\text{ds}} I_{\text{on}} t_{\text{on}} + V_{\text{ds}} I_{\text{off}} t_{\text{off}}) \times \frac{f_s}{2} \quad (23)$$

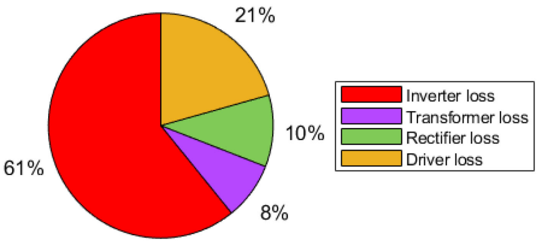

Fig. 23. Distribution diagram of system loss under rated condition.

where t_{ON} and t_{OFF} represent the time of the turn-ON transition and the time of the turn-OFF transition, respectively. V_{ds}, I_{ON}, and I_{OFF} represent the voltage across the switch, the value of turn-ON current, and the value of turn-OFF current, respectively.

So the inverter loss can be calculated as follows:

$$P_{\mathrm{inv}} = P_{\mathrm{cond}} + P_{\mathrm{sw}}. \tag{24}$$

The loss of rectifier can be obtained by [31]

$$P_{\mathrm{rec}} = N_{\mathrm{sw}} D_{\mathrm{rec}} U_{\mathrm{sw}} I_{\mathrm{sw}} \tag{25}$$

where N_{sw} represent the number of switch of the rectifier, D_{rec} represent the duty cycle of the switch in the rectifier, U_{sw} represent the forward conduction voltage of the switch, and I_{sw} represent the current flowing through the switch.

The loss of transformer can be calculated as follows:

$$P_{\mathrm{tra}} = I_{\mathrm{pri}}^2 R_{\mathrm{pri}} + I_{\mathrm{sec}}^2 R_{\mathrm{sec}} \tag{26}$$

where I_{pri} and I_{sec} are the current rms value flowing through the primary winding and secondary winding, respectively. R_{pri} and R_{sec} are the resistance of the primary winding and secondary winding, respectively, and

$$P_{\mathrm{dri}} = V_{\mathrm{dri}} \times Q_G \times f_s \tag{27}$$

where V_{dri} and Q_G are the amplitude of the gate drive waveform and the total gate charge, respectively.

Under the rated condition, the inverter loss is 5.9 W, the rectifier loss is 1 W, the transformer loss is 0.8 W, and the drive loss is 2 W. Fig. 23 shows the loss ratio of each part.

V. CONCLUSION

In this article, a 10 MHz dc/dc converter based on 3-D air core transformer is designed, which aims for the challenge that there is no available analog controller for synchronous rectification that can operate at such high frequency. By using the characteristics of no leakage inductance of the nested toroidal air core transformer, the phase difference between converter's output voltage and rectifier's input voltage can be regulated as zero, so that the rectifier and the inverter can use the same signal to drive switches, which simplifies the control of the synchronous rectification and improve the system performance. Both primary compensation and secondary compensation can achieve zero phase difference. For primary resonant circuit with 50 V input voltage, the efficiency is 74.5%. Compared with air core PCB transformer with leakage inductance, the efficiency can be improved by 6.8%.

REFERENCES

[1] J. M. Alonso, G. Martínez, M. Perdigão, M. R. Cosetin, and R. N. do Prado, "A systematic approach to modeling complex magnetic devices using SPICE: Application to variable inductors," *IEEE Trans. Power Electron.*, vol. 31, no. 11, pp. 7735–7746, Nov. 2016.

[2] Y. Guan, C. Liu, Y. Wang, W. Wang, and D. G. Xu, "Analysis and design of a high frequency low-profile converter for bendable equipment," *IEEE Trans. Power Electron.*, to be published.

[3] B. Sun, Z. Zhang, and M. A. E. Andersen, "A comparison review of the resonant gate driver in the silicon MOSFET and the GaN transistor application," *IEEE Trans. Ind. Appl.*, vol. 55, no. 6, pp. 7776–7786, Nov./Dec. 2019.

[4] Y. Guan, C. Liu, Y. Wang, W. Wang, and D. Xu, "Analytical derivation and design of 20-MHz DC–DC soft-switching resonant converter," *IEEE Trans. Ind. Electron.*, vol. 68 no. 1, pp. 210–221, Jan. 2021.

[5] N. Huang *et al.*, "Power quality disturbances classification using rotation forest and multi-resolution fast S-transform with data compression in time domain," *IET Gener. Transmiss. Distrib.*, vol. 13, no. 22, pp. 5091–5101, Nov. 2019.

[6] D. J. Perreault *et al.*, "Opportunities and challenges in very high frequency power conversion," in *Proc. 24th Annu. IEEE Appl. Power Electron. Conf. Expo.*, 2009, pp. 1–14.

[7] S. Park and J. Rivas-Davila, "Duty cycle and frequency modulations in class-e dc–dc converters for a wide range of input and output voltages," *IEEE Trans. Power Electron.*, vol. 33, no. 12, pp. 10524–10538, Dec. 2018.

[8] H. Park and J. Jung, "Power stage and feedback loop design for LLC resonant converter in high-switching-frequency operation," *IEEE Trans. Power Electron.*, vol. 32, no. 10, pp. 7770–7782, Oct. 2017.

[9] A. Knott *et al.*, "Evolution of very high frequency power supplies," *IEEE J. Emerg. Sel. Topics Power Electron.*, vol. 2, no. 3, pp. 386–394, Sep. 2014.

[10] M. Liu, M. Fu, and C. Ma, "Parameter design for a 6.78-MHz wireless power transfer system based on analytical derivation of class E current driven rectifier," *IEEE Trans. Power Electron.*, vol. 31, no. 6, pp. 4280–4291, Jun. 2016.

[11] L. Olivia, "Radio frequency dc–dc converters: Device characterization, topology evaluation, and design," Ph.D. dissertation, Dept. Elect. Eng. Comput. Sci., Massachusetts Inst. Technol., Cambridge, MA, USA, 2008.

[12] R. C. N. Pilawa-Podgurski, "Design and evaluation of a very high frequency dc/dc converter," M.Eng. thesis, Dept. Elect. Eng. Comput. Sci., Massachusetts Inst. Technol., Cambridge, MA, USA, 2007.

[13] J. W. Phinney, "Multi-resonant passive components for power conversion," Ph.D. dissertation, Dept. Elect. Eng. Comput. Sci., Massachusetts Inst. Technol., Cambridge, MA, USA, Jun. 2005.

[14] J. Zhang, J. Liao, J. Wang, and Z. Qian, "A current-driving synchronous rectifier for an LLC resonant converter with voltage-doubler rectifier structure," *IEEE Trans. Power Electron.*, vol. 27, no. 4, pp. 1894–1904, Apr. 2012.

[15] "SRK2000A: Synchronous rectifier smart driver for LLC and resonant converters," STMicroelectronics, May 2017. [Online]. Available: https://www.st.com/resource/en/datasheet/srk2000a.pdf

[16] D. Fu, Y. Liu, F. C. Lee, and M. Xu, "A novel driving scheme for synchronous rectifiers in LLC resonant converters," *IEEE Trans. Power Electron.*, vol. 24, no. 5, pp. 1321–1329, May 2009.

[17] F. Wang, B. A. McDonald, J. Langham, and B. Fan, "A novel adaptive synchronous rectification method for digitally controlled LLC converters," in *Proc. IEEE Appl. Power Electron. Conf. Expo.*, 2016, pp. 334–338.

[18] R. Blanchard and P. E. Thibodeau, "The design of a high efficiency, low voltage power supply using mosfet synchronous rectification and current mode control," in *Proc. IEEE Power Electron. Specialists Conf.*, Jun. 1985, pp. 355–361.

[19] M. Jovanovic, M. Zhang, and F. Lee, "Evaluation of synchronous rectification efficiency improvement limits in forward converters," *IEEE Trans. Ind. Electron.*, vol. 42, no. 4, pp. 387–395, Aug. 1995.

[20] S. Xu, Q. Qian, T. Tao, L. Yu, S. Lu, and W. Sun, "Synchronous rectification using resonant capacitor voltage for secondary side resonant active clamp flyback converter," in *Proc. IEEE Appl. Power Electron. Conf. Expo.*, 2020, pp. 2926–2931.

[21] X. Ren, Y. Zhou, D. Wang, X. Zou, and Z. Zhang, "A 10-MHz isolated synchronous class$-\Phi_2$ resonant converter," *IEEE Trans. Power Electron.*, vol. 31, no. 12, pp. 8317–8328, Jan. 2016.

[22] J. Pedersen, M. Madsen, A. Knott, and M. Andersen, "Self-oscillating galvanic isolated bidirectional very high frequency dc-dc converter," in *Proc. 30th Annu. IEEE Appl. Power Electron. Conf. Expo.*, 2015, pp. 1974–1978.

[23] Z. Tong, W. D. Braun, and J. M. Rivas-Davila, “Design and fabrication of three-dimensional printed air-core transformers for high-frequency power applications,” *IEEE Trans. Power Electron.*, vol. 35, no. 8, pp. 8472–8489, Aug. 2020.

[24] W. G. Hurley, M. C. Duffy, J. Zhang, I. Lope, B. Kunz, and W. H. Wölfle, “A unified approach to the calculation of self- and mutual-inductance for coaxial coils in air,” *IEEE Trans. Power Electron.*, vol. 30, no. 11, pp. 6155–6162, Nov. 2015.

[25] K. Lee, E. Chung, Y. Han, and J. Ha, “A family of high-frequency single-switch dc–dc converters with low switch voltage stress based on impedance networks,” *IEEE Trans. Power Electron.*, vol. 32, no. 4, pp. 2913–2924, Apr. 2017.

[26] I. O. Lee and G. W. Moon, “The k-Q analysis for an LLC series resonant converter,” *IEEE Trans. Power Electron.*, vol. 29, no. 1, pp. 13–16, Jan. 2014.

[27] U. Kundu, K. Yenduri, and P. Sensarma, “Accurate ZVS analysis for magnetic design and efficiency improvement of fullbridge LLC resonant converter,” *IEEE Trans. Power Electron.*, vol. 32, no. 3, pp. 1703–1706, Mar. 2017.

[28] S. Ramo, J. Whinnery, and T. V. Duzer, *Fields and Waves in Communication Electronics*, 3rd ed. Hoboken, NJ, USA: Wiley, 1994.

[29] S. Zong, H. Luo, W. Li, Y. Deng, and X. He, “Asymmetrical duty cycle-controlled LLC resonant converter with equivalent switching frequency doubler,” *IEEE Trans. Power Electron.*, vol. 31, no. 7, pp. 4963–4973, Jul. 2016.

[30] E. Chen and A. Leng, *Power MOSFET Switching Loss Precise Analysis*. Taipei, Taiwan: Niko Semiconductor Co, Ltd, Aug. 2010.

[31] N. Mohan, T. M. Undeland, and W. P. Robbins, *Power Electronics: Converters, Applications, and Design*, 3rd ed. Hoboken, NJ, USA: Wiley, 2003.

Yueshi Guan (Member, IEEE) was born in Heilongjiang Province, China, in 1990. He received the B.S., M.S., and Ph.D. degrees in electrical engineering from Harbin Institute of Technology (HIT), Harbin, China, in 2013, 2015, and 2019, respectively.

Since 2019, he has been an Associate Professor with the Department of Electrical and Electronics Engineering, HIT. His research interests include high-frequency and very-high-frequency converters, single-stage ac/dc converter, and high conversion ratio converters.

Zhenyu Shi (Student Member, IEEE) was born in Liaoning Province, China, in 1998. He received the B.S. degree in electrical engineering in 2020 from Harbin Institute of Technology, Harbin, China, where he is currently working toward the M.S. degree in electrical engineering.

His research interests include high-frequency and very-high-frequency dc/dc converters.

Chang Liu (Student Member, IEEE) was born in Jilin Province, China, in 1997. She received the B.S. degree in electrical engineering in 2019 from Harbin Institute of Technology, Harbin, China, where she is currently working toward the M.S. degree in electrical engineering.

Her research interests include high-frequency and very-high-frequency converters.

Yijie Wang (Senior Member, IEEE) was born in Heilongjiang Province, China, in 1982. He received the B.S., M.S., and Ph.D. degrees in electrical engineering from Harbin Institute of Technology, Harbin, China, in 2005, 2007, and 2012, respectively.

From 2012 to 2014, he was a Lecturer with the Department of Electrical and Electronics Engineering, Harbin Institute of Technology. Since 2015, he has been an Associate Professor with the Department of Electrical and Electronics Engineering, Harbin Institute of Technology. His research interests include dc–dc converters, soft-switching power converters, power factor correction circuits, digital control electronic ballasts, and LED lighting systems.

Dianguo Xu (Fellow, IEEE) was born in Heilongjiang, China, in 1960. He received the B.S. degree in control engineering from Harbin Engineering University, Harbin, China, in 1982, and the M.S. and Ph.D. degrees in electrical engineering from Harbin Institute of Technology (HIT), Harbin, China, in 1984 and 1989, respectively.

In 1984, he joined the Department of Electrical Engineering, HIT as an Assistant Professor. Since 1994, he has been a Professor with the Department of Electrical Engineering, HIT. He was the Dean with the School of Electrical Engineering and Automation, HIT, from 2000 to 2010, and is currently the Vice President with HIT. He has authored/coauthored more than 600 technical papers. His research interests include renewable energy generation technology, power quality mitigation, sensorless vector controlled motor drives, and high-performance servo system.

Prof. Xu is an Associate Editor of the IEEE TRANSACTIONS ON INDUSTRIAL ELECTRONICS and the IEEE JOURNAL OF EMERGING AND SELECTED TOPICS IN POWER ELECTRONICS. He serves as Chairman of IEEE Harbin Section.